arXiv:1610.04036v1 [cond-mat.mes-hall] 13 Oct 2016

Coulomb-blockade and Pauli-blockade magnetometry

Gábor Széchenyi[1] and András Pályi[1,2]

[1] *Institute of Physics, Eötvös University, Budapest, Hungary*
[2] *MTA-BME Condensed Matter Research Group and Department of Physics, Budapest University of Technology and Economics, Budapest, Hungary*

(Dated: October 14, 2016)

Scanning-probe magnetometry is a valuable experimental tool to investigate magnetic phenomena at the micro- and nanoscale. We theoretically analyze the possibility of measuring magnetic fields via the electrical current flowing through quantum dots. We characterize the shot-noise-limited magnetic-field sensitivity of two devices: a single dot in the Coulomb blockade regime, and a double dot in the Pauli blockade regime. Constructing such magnetometers using carbon nanotube quantum dots would benefit from the large, strongly anisotropic and controllable g tensors, the low abundance of nuclear spins, and the small detection volume allowing for nanoscale spatial resolution; we estimate that a sensitivity below 1 $\mu\mathrm{T}/\sqrt{\mathrm{Hz}}$ can be achieved with this material. As quantum dots have already proven to be useful as scanning-probe electrometers, our proposal highlights their potential as hybrid sensors having in situ switching capability between electrical and magnetic sensing.

PACS numbers: 07.55.Ge, 73.63.Kv, 73.63.Fg, 73.23.Hk

I. INTRODUCTION

The detection of weak magnetic fields with high spatial resolution is a task of great importance in diverse areas, from fundamental physics and chemistry to practical applications in data storage and medical imaging. This task can be tackled by scanning-probe magnetic-field sensors, based on various operating principles.[1–10] Low-temperature scanning-probe magnetometry has been successfully used to image a range of nontrivial magnetic phenomena, e.g., vortices in superconductors,[11–13] exotic magnetic structures,[8,14,15] and current-induced magnetic fields in various systems[16,17] including topological insulators.[18,19] The applicability of the different magnetic-field sensors (SQUIDs, Hall bars, NV centers, etc) for specific tasks is determined by a number of characteristics, including magnetic-field sensitivity and detection volume, the latter one related to the achievable spatial resolution. A key challenge is to improve the capabilities of these sensors, either by advancing existing designs, or by devising completely new principles and devices.

In this work, we propose and theoretically explore two quantum-dot-based low-temperature approaches to magnetic-field sensing, offering a combination of sub-$\mu\mathrm{T}/\sqrt{\mathrm{Hz}}$ magnetic-field sensitivity, nanoscale spatial resolution, and conceptual simplicity via all-electrical and all-dc operation (i.e., optical or high-frequency electronic elements are not required). In both devices, the magnetic field is measured by measuring the electric current through the dots. The first, simpler device we study is a single quantum dot in the Coulomb blockade regime; the second one is a double quantum dot (DQD) in the Pauli blockade regime.[20] Our main goal is to determine the fundamental limits on the achievable magnetic-field sensitivity of these sensors by considering the effects of shot noise and the thermal broadening of the electron distributions in the contacts. We also discuss the effect of electric potential fluctuations on the sensitivity, and highlight the advantages of carbon nanotubes (CNTs) for realizing the proposed magnetometry principle.

II. SENSITIVITY OF A CURRENT-BASED MAGNETOMETER

Before presenting the concrete magnetometry schemes, we first characterize the shot-noise-limited sensitivity of a generic magnetometer that is based on the magnetic-field dependence $I(\boldsymbol{B})$ of the steady-state electric current flowing through a mesoscopic conductor. We wish to exploit this dependence for measuring small deviations $\delta\boldsymbol{B}$ of the magnetic field from a pre-set 'offset field' or 'working point' $\boldsymbol{B}_0$. We focus on the generic situation when the current is linearly sensitive to a single Cartesian component of $\delta\boldsymbol{B}$, say, δB_z; that is, $I'(\boldsymbol{B}_0) \equiv \frac{\partial I}{\partial B_z}\Big|_{\boldsymbol{B}_0} > 0$, and $\frac{\partial I}{\partial B_x}\Big|_{\boldsymbol{B}_0} = \frac{\partial I}{\partial B_y}\Big|_{\boldsymbol{B}_0} = 0$. This is always fulfilled if we align the z axis with the gradient vector of $I(\boldsymbol{B})$ at $\boldsymbol{B}_0$. In this case, the device can be operated as a linear detector of δB_z. In analogy with the sensitivity formula for a current-based electrometer,[21] we claim that the magnetic-field sensitivity of the magnetometer is characterized by the quantity

$$S(\boldsymbol{B}_0) = \frac{\sqrt{eF(\boldsymbol{B}_0)I(\boldsymbol{B}_0)}}{I'(\boldsymbol{B}_0)}, \tag{1}$$

where e is the absolute value of the electron's charge, and F is the Fano factor,[22] defined as the ratio of the shot noise and the current. For more details, see Appendix A. In what follows, we will refer to the shot-noise-limited sensitivity S as the sensitivity.

The dimension of S is $\mathrm{T}/\sqrt{\mathrm{Hz}}$. A smaller value of S implies the ability of resolving smaller differences in δB_z in a given measurement time window; that is, an

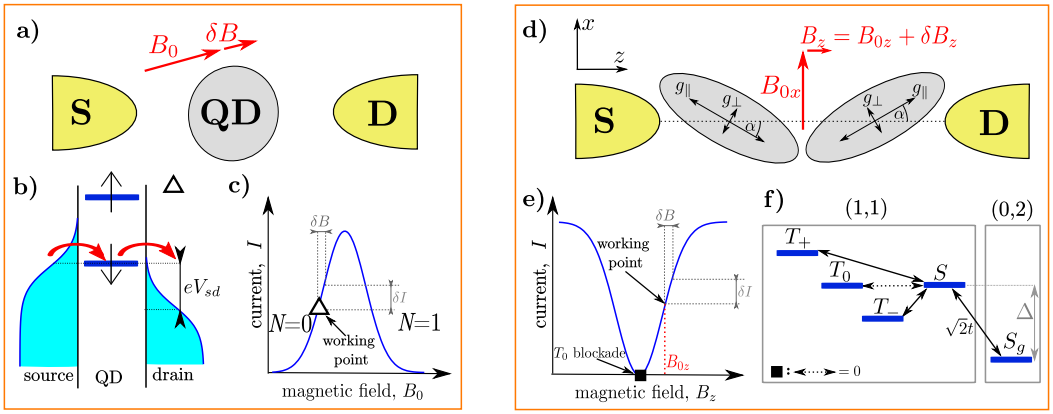

FIG. 1. (Color online) Coulomb-blockade and Pauli-blockade magnetometry. (a) Coulomb-blockaded single-level quantum dot between source (S) and drain (D). The spin states are split by an offset magnetic field B_0 setting the working point. (b,c) Current is flowing through the $\downarrow$ state, therefore the current changes by δI if the energy of $\downarrow$ is changed by a small variation δB of the magnetic field. This allows for measuring δB via measuring the current. The shaded areas in (b) represent the thermally broadened electronic Fermi-Dirac distributions in the contacts. (d) Pauli-blockaded double quantum dot. The two ellipsoids represent the g-tensors on the two dots. The g-tensors are anisotropic, and have misaligned principal axes in the two dots, enclosing the misalignment angle 2α. The working point of the magnetometer is set by the field $\boldsymbol{B}_0 = (B_{0x}, 0, B_{0z})$, and δB_z is measured via measuring the change δI [see (e)] in the current flowing through the dots. (e) Current as a function of B_z. Black square (■) denotes the point of T_0 blockade. (f) Two-electron level diagram in the vicinity of T_0 blockade. Solid and dotted black arrows represent magnetic-field-induced coupling matrix elements. At the T_0 blockade (■), the T_0-S coupling (dotted black arrow) vanishes.

improved performance. Equation (1) is in line with the expectation that the sensitivity is improved if the noise is suppressed (F is decreased) or if the dependence of the current on the magnetic field is enhanced ($I'(\boldsymbol{B}_0)$ is increased).

III. COULOMB-BLOCKADE MAGNETOMETRY

Here, we describe and characterize a principle of magnetometry based on Zeeman-splitting-induced changes in the current flowing through a single dot, as sketched in Fig. 1a,b,c. The scheme is analogous to the electrometer described in Refs. 21 and 23.

The dot, shown schematically in Fig. 1a, is gate-voltage-tuned to the vicinity of a Coulomb peak, and a finite magnetic field $\boldsymbol{B}_0 = (0, 0, B_0)$ creates a large Zeeman splitting $g\mu_B B_0$, where g is the material-dependent effective g-factor of the electron. The Zeeman splitting separates the singly occupied $\uparrow$ (spin-up) excited state from the $\downarrow$ (spin-down) ground state, as shown in Fig. 1b. A plunger gate voltage and a small source-drain bias voltage can be used to tune the energy levels such that $\downarrow$ is in the source-drain bias window as shown in Fig. 1b. Then the current flows via sequential tunneling through the transport cycle $0 \rightarrow\downarrow\rightarrow 0$, where 0 corresponds to an empty dot, and $I(B_0)$ is set to the slope of the Coulomb-peak, see the working point in Fig. 1c. Then, a small δB increase in the z component of the magnetic field lowers the energy of the current-carrying $\downarrow$ state by $g\mu_B\delta B$, and therefore increases the current flowing through the dot by the amount δI as shown in Fig. 1c; measuring this increase δI of the current will reveal δB.

This measurement scheme is directionally sensitive in the following sense. Assume that the small change in the magnetic field has all three Cartesian components, $\delta\boldsymbol{B} = (\delta B_x, \delta B_y, \delta B_z)$, and it is much weaker than the offset field, $\delta B \ll B_0$. Then the Zeeman splitting $g\mu_B\sqrt{(B_0+\delta B_z)^2 + \delta B_x^2 + \delta B_y^2}$ is well approximated by $g\mu_B\left(B_0 + \delta B_z + \frac{\delta B^2}{2B_0}\right)$, that is, it is mainly determined by the component δB_z along the offset field.

Now we use simple considerations to estimate the parameter dependence of the sensitivity S, and argue that the temperature has a strong influence on the optimal sensitivity: the latter is degraded as T is increased. For these considerations, we introduce the characteristic rate Γ, describing the tunnel coupling of the dot to the source and drain leads. We propose that at a given T, (i) the sensitivity is optimized if $h\Gamma$ is comparable to k_BT, and (ii) the order of magnitude of the optimal sensitivity is estimated as

$$S_{\rm opt} \sim \frac{\sqrt{hk_BT}}{g\mu_B}. \qquad (2)$$

The reasoning is as follows. The height of the Coulomb peak is set by the lead-dot tunneling rate Γ, $I \sim e\Gamma$, whereas the Fano factor is $F \sim 1$. The slope of the Coulomb peak can be set by thermal broadening or tun-

nel broadening: $I' \sim \frac{e\Gamma}{\max\{h\Gamma, k_BT\}/g\mu_B}$. Then, Eq. (1) implies $S \sim \frac{\max\{h\Gamma, k_BT\}}{g\mu_B\sqrt{\Gamma}}$. On the one hand, this has the consequence that for slow tunneling, $\Gamma < k_BT$, the sensitivity $S \propto 1/\sqrt{\Gamma}$ decreases with increasing Γ; on the other hand, for fast tunneling $\Gamma > k_BT$, the sensitivity $S \propto \sqrt{\Gamma}$ increases with increasing Γ. These imply claims (i) and (ii). Using the estimate in Eq. (2) and the values $g = 30$, achievable in clean CNT dots,[24–27] and $T = 50\,\mathrm{mK}$, we find $S_{\mathrm{opt}} \sim 77\,\mathrm{nT}/\sqrt{\mathrm{Hz}}$.

Now we go beyond the previous estimate and quantify the magnetic-field sensitivity of the Coulomb-blockade magnetometry via a simple model. The single-electron Hamiltonian of the quantum dot involves the on-site energy ϵ and the Zeeman term: $H_{\mathrm{CBM}} = \epsilon + \frac{1}{2}g\mu_B B\sigma_z$, where g is the effective g factor, μ_B is the Bohr magneton, and B is the magnetic field. The electronic Fermi-Dirac distributions in the source and drain leads are characterized by their common temperature T and symmetrically biased chemical potentials $\mu_L = -\mu_R = eV_{sd}/2$ with V_{sd} being the source-drain bias voltage. Lead-dot tunneling rates are set by the rate Γ, the level positions, and the Fermi-Dirac distributions of the leads. We describe the transport process by a classical master equation, neglecting double occupancy of the dot. The current I and the Fano factor F is evaluated using the counting-field method;[28,29] details can be found in Appendix C. From these, the magnetic-field sensitivity S is calculated from Eq. (1).

Figures 2a,c,d shows the calculated current I, Fano factor F and magnetic-field sensitivity S, respectively, as functions of the offset field B_0 and the on-site energy ϵ of the dot, for a given parameter set (see caption) where the thermal energy scale k_BT dominates the tunneling energy scale $h\Gamma$. Figure 2b shows a horizontal cut of the current, $I(B_0, \epsilon = 20\,\mathrm{meV})$, along the blue horizontal line in Fig. 2a. The dark spot in the centre of Fig. 2a, at $\epsilon \approx 0$ and $B_0 \approx 0$, is a finite-bias Coulomb peak, where the two spin levels $\downarrow$ and $\uparrow$ are approximately degenerate, both of them is located within the bias window, and hence both contributes to the current. The dark diagonal lines forming the V-shaped region in Fig. 2a correspond to Coulomb peaks where the current is carried by a single spin level, as shown in Fig 1b: a Zeeman splitting $g\mu_B B_0 > k_BT, eV_{sd}$ exceeding the thermal and voltage broadening is induced between the spin levels by the offset field B_0, thereby only the lower-energy spin level contributes to the current.

The typical values of the Fano factor in Fig. 2c corroborate our above estimate $F \sim 1$, and implies that the Fano factor plays a minor role in determining the order of magnitude of the magnetic-field sensitivity. The sensitivity in Fig. 2d is therefore following a pattern which can essentially be deduced from the pattern of the current, Fig. 2a: the sensitivity is good, that is, S is small, wherever the derivative of the current with respect to the offset field is appreciable; that is, along the two slopes of the V-shaped high-current regions of Fig. 2a. In Fig. 2d,

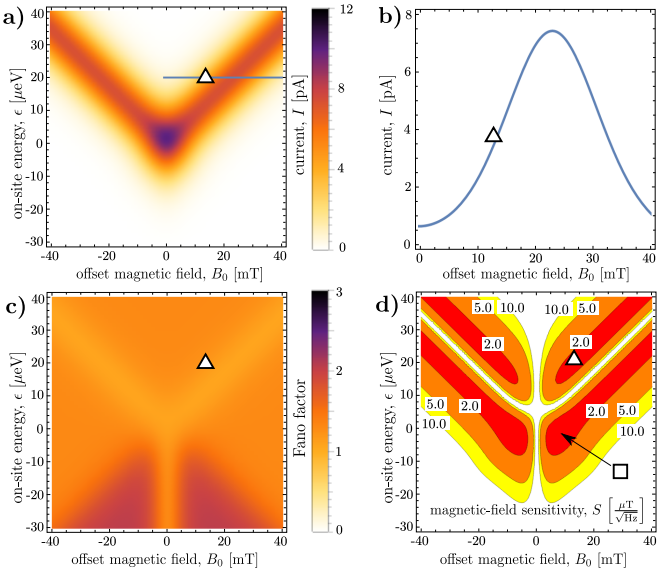

FIG. 2. Coulomb-blockade magnetometry: Magnetic-field sensitivity of a single quantum dot. (a,b) Current, (c) Fano factor, and (d) sensitivity of a Coulomb-blockade magnetometer. (b) Magnetic-field dependence of the current along the blue line ($\epsilon = 20\,\mu$eV) in (a). The white triangle $\triangle$ denotes a local minimum of the sensitivity S along the blue line in (a). The optimal value of sensitivity denoted by the white square $\square$ is $S = 1.4\ \mu\mathrm{T}/\sqrt{\mathrm{Hz}}$. Parameters: $V_{sd} = 8.6\,\mu$V, $k_BT = 4.3\,\mu$eV ($T \approx 50$ mK), $h\Gamma = 0.86\,\mu$eV ($\Gamma \approx 200$ MHz, $e\Gamma \approx 33\,$pA), $g = 30$.

the sensitivity has a local minimum $S = 1.7\,\mu\mathrm{T}/\sqrt{\mathrm{Hz}}$ at the white triangle.

Note that in Fig. 2d, the global minimum of the magnetic-field sensitivity is at the working point marked by the white square ($\square$), which corresponds to $(\epsilon, B_0) \approx (0\ \mu\mathrm{eV}, 10\ \mathrm{mT})$. At $\square$, the value of the sensitivity is $S = 1.4\ \mu\mathrm{T}/\sqrt{\mathrm{Hz}}$. We emphasize that the operation of the magnetometer at this working point $\square$ is not following the scheme that we outlined above and visualized in Fig. 1b. The scheme of operation in the working point $\square$ is discussed in detail in Appendix B. In Appendix B, we also argue that by choosing an appropriate working point in the vicinity of $\square$, the sensitivity-degrading effects of electric potential fluctuations can be mitigated.

To conclude, we argued that the fundamental limit on the magnetic-field sensitivity of a Coulomb-blockade magnetometer is set by the temperature, evaluated and analyzed the magnetic-field sensitivity of such a device using a simple model, and estimated that at experimentally available low temperatures, and with a large g-factor, e.g., offered by CNT dots, the optimal magnetic-field sensitivity can be below $\mu\mathrm{T}/\sqrt{\mathrm{Hz}}$.

IV. PAULI-BLOCKADE MAGNETOMETRY

Here, we describe an alternative magnetometer based on a DQD operated in the Pauli blockade regime.[20] In such DQDs, the magnetic-field dependence of the current can be caused by various mechanisms, e.g., hyperfine interaction[30,31] or spin-orbit interaction.[32,33] Here, we focus on one particular mechanism, where the magnetic-field dependence of the current is governed by the different and strongly anisotropic g-tensors in the two dots, as depicted in Fig. 1d. We will show that if we have this feature in the device, then the magnetic-field sensitivity is optimized in the close vicinity of a special setting that we call the 'T_0 blockade' (see Fig. 1e,f, and below). Based on a comparison of a recent experiment[34] and our corresponding theoretical results,[35] we argue that DQDs in bent CNTs provide an opportunity to meet these requirements.

In the Pauli-blockade regime, a large dc source-drain voltage is applied to a serially coupled DQD, and a dc current might flow via the transport cycle $(0,1) \to (1,1) \to (0,2) \to (0,1)$, where $(N_L,\ N_R)$ denotes the number of electrons in the left and right dots. The $(1,1) \to (0,2)$ transition is blocked due to Pauli's exclusion principle if a (1,1) triplet state becomes occupied during the transport process, leading to a complete suppression of the current. We describe the DQD by the two-electron Hamiltonian[31] $H = H_B + H_{\rm tun} + H_\Delta$. The interaction of the external homogeneous magnetic field and the electron spins is

$$H_B = \frac{1}{2}\mu_B \boldsymbol{B} \cdot \left(\hat{\mathbf{g}}_L \boldsymbol{\sigma}_L + \hat{\mathbf{g}}_R \boldsymbol{\sigma}_R\right). \tag{3}$$

Here, $\boldsymbol{\sigma}_{L/R}$ is the vector of Pauli matrices representing the spins of the electrons. The g-tensors $\hat{\mathbf{g}}_L$ and $\hat{\mathbf{g}}_R$ are assumed to have the same principal values $g_\perp$, $g_\perp$, $g_\parallel$ in the dots L and R. (This is not a strict requirement, as we discuss in section V D.) Furthermore, the principal axes of the g-tensors enclose a small angle $2\alpha \ll 1$, as shown in Fig. 1d. Choosing the coordinate system as depicted in Fig. 1d, the g-tensors are given as $\hat{\mathbf{g}}_D = g_\parallel \boldsymbol{t}_D \circ \boldsymbol{t}_D + g_\perp \left(1 - \boldsymbol{t}_D \circ \boldsymbol{t}_D\right)$, where $\boldsymbol{t}_D = (D\sin\alpha, 0, \cos\alpha)$ is the unit vector pointing along the local principal axis of $g_\parallel$ in dot $D \in (L,R) \equiv (-1,1)$. Spin-conserving tunneling between the dots is represented by $H_t = \sqrt{2}t(|S_g\rangle\langle S| + |S\rangle\langle S_g|)$, where S $[S_g]$ is the singlet state in the (1,1) [(0,2)] charge configuration. The last term $H_\Delta = -\Delta|S_g\rangle\langle S_g|$ describes the energy detuning between the (1,1) and (0,2) charge configurations. Finally, the incoherent tunneling processes from the source electrode to dot L (from dot R to the drain electrode) are characterized by the rate Γ_L (Γ_R).

In this model, the T_0 blockade appears in the case when the magnetic field is aligned with the x axis, $\boldsymbol{B} = (B,0,0)$. Then, taking the spin quantization axis along x, which coincides with the direction of $\boldsymbol{B}$ as well as with that of the average effective magnetic field $\frac{1}{2}\left(\hat{\mathbf{g}}_L + \hat{\mathbf{g}}_R\right)\boldsymbol{B}$, the (1,1) triplet state $|T_0\rangle = \frac{1}{\sqrt{2}}\left(|\uparrow\downarrow\rangle + |\downarrow\uparrow\rangle\right)$ is an energy eigenstate, implying that it is decoupled from the (0,2) charge configuration and therefore blocks the current.[31] This setting is indicated in Fig. 1e and f by the black square (■). The other four two-electron energy eigenstates all contain a finite (0,2) component and therefore can decay to the single-electron states by emitting an electron to the drain; hence we call this special case the T_0 blockade. Note that the appearance of the T_0 blockade does not require the equality of the g-tensor principal values in the two dots, see section V D.

Importantly, the T_0 blockade is maintained as long as the magnetic field lies in the xy plane. It is however lifted by a finite B_z component, as the latter couples T_0 to the singlet states.[31] Therefore, in the vicinity of the T_0 blockade, the current is mostly determined by B_z. The decay rate of $\bar{T}_0$, that is, the energy eigenstate that evolves from T_0 as B_z is turned on, is given by $\bar{\Gamma} = 2\Gamma_R \left|\langle S_g|\bar{T}_0\rangle\right|^2$. We express $\bar{T}_0$ using first-order perturbation theory in $\mu_B g_\parallel B_z$, see Appendix D. After a leading-order expansion in the small angle α, and assuming $g_\perp \ll g_\parallel$, fulfilled by the realistic parameter set used below, we find

$$\left|\langle S_g|\bar{T}_0\rangle\right|^2 = \left(\frac{\mu_B g_\parallel B_z}{\sqrt{2}t}\frac{g_\parallel}{g_\perp}\alpha\right)^2. \tag{4}$$

Note that this result is independent of the (1,1)-(0,2) energy detuning Δ; the consequences of this are discussed in section V C.

Assuming that $\bar{\Gamma}$ is the smallest tunnel rate in the transport process, and making use of the formalism of Refs. 28 and 29, we can express the current as

$$I = 4e\bar{\Gamma} = 8e\Gamma_R \left(\frac{\mu_B g_\parallel B_z}{\sqrt{2}t}\frac{g_\parallel}{g_\perp}\alpha\right)^2, \tag{5}$$

and the Fano factor as

$$F = 7. \tag{6}$$

Details can be found in Appendix C.

The dependence $I(B_z)$ can be utilized for current-based magnetometry. Take an offset field with a small z component, $\boldsymbol{B}_0 = (B_{0x}, 0, B_{0z})$. Consider the task that a small change δB_z in the z component of the field should be detected via measuring the current. The corresponding shot-noise-limited sensitivity for the device operated in the vicinity of the T_0 blockade can be expressed from Eqs. (1), (5) and (6):

$$S = \frac{\sqrt{7}}{4}\frac{t g_\perp}{\alpha \mu_B g_\parallel^2}\frac{1}{\sqrt{\Gamma_{\rm R}}}. \tag{7}$$

For the parameter set $g_\parallel = 30$, $g_\perp = 1$, $\Gamma_R = 1$ GHz, $t = 5$ μeV, $\alpha = 3°$, realistic for a clean CNT DQD,[34–36] Eq. (7) implies a sensitivity of $S \approx 37 \frac{\rm nT}{\sqrt{\rm Hz}}$.

To explore the achievable magnetic-field sensitivity of the device in a broader magnetic-field range, and to corroborate our perturbative results discussed so far, we numerically calculated the current, the Fano factor, and

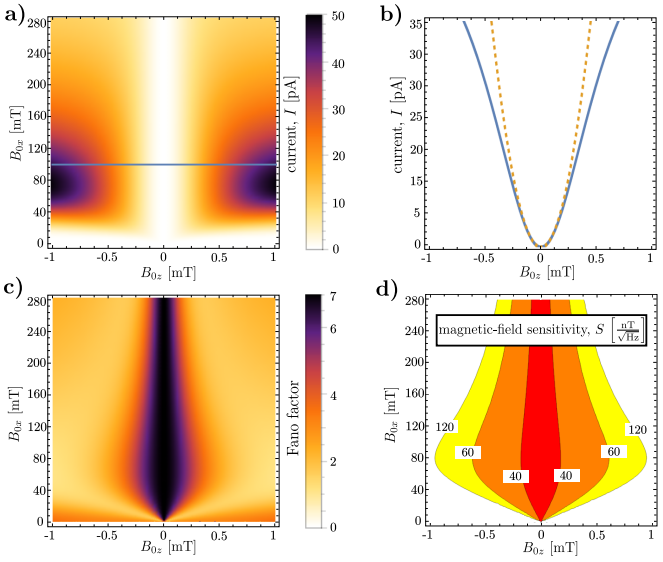

FIG. 3. (Color online) Pauli-blockade magnetometry: Magnetic-field sensitivity of a double quantum dot. Numerically calculated (a) current, (c) Fano factor, and (d) magnetic-field sensitivity. The suppressed current around $B_{0z} = 0$ in (a) is due to T_0 blockade. (b) Blue line shows the horizontal cut along the blue line ($B_{0x} = 100$ mT) in (a). Dashed orange line shows the corresponding perturbative result Eq. (5). The optimal value of the sensitivity in (d) is $S_{\rm opt} = 37$ nT/$\sqrt{\rm Hz}$, at the point $(B_{0z}, B_{0x}) = (0, 25)$ mT. Parameters: $g_\parallel = 30$, $g_\perp = 1$, $\Gamma_R = \Gamma_L = 1$ GHz, $t = 5\ \mu$eV, $\Delta = 0\,\mu$eV, $\alpha = 3^\circ$.

the sensitivity. The dependence of these quantities on the offset magnetic field are shown in Fig. 3a,c and d, respectively, for the parameter values given in the figure caption. In Fig. 3b, the blue solid line shows the current along the horizontal cut in Fig. 3a, whereas the orange dashed line shows the corresponding perturbative result Eq. (5). The numerical results in Fig. 3 do confirm our analytical results obtained for the vicinity of the T_0 blockade, $B_{0z} \approx 0$: On the one hand, the two curves coincide in that region in Fig. 3b; on the other hand, the maximum of the Fano factor in Fig. 3c is indeed $F = 7$ as predicted by Eq. (6).

The key features of the results in Fig. 3 are the following. (i) Figure 3a shows that the current is blocked at $B_{0z} = 0$; that is the T_0 blockade. In its vicinity, the current shows a quadratic dependence of B_{0z}, as testified by the line cut in Fig. 3b and our perturbative result Eq. (5), and essentially no dependence on B_{0x}. This implies that indeed, the device as a magnetometer is directionally sensitive, that is, variations of the current are caused by variations of the z component of the external magnetic field only. (ii) Fig. 3d shows that the best sensitivities are achieved in the vicinity of the central vertical region (black), which indeed roughly coincides with the T_0 blockade region, i.e., the white vertical region with suppressed current in Fig. 3a and the dark $F \approx 7$ vertical region in the Fano factor plot Fig. 3c. (iii) The current in Fig. 3 shows maxima around $(B_{0z}, B_{0x}) = (\pm 1\,\text{mT}, 80\,\text{mT})$. The reason for this is that singlet-triplet mixing is most efficient in these magnetic-field ranges. At these dark spots, the local effective magnetic fields $\hat{g}_L \boldsymbol{B}$ and $\hat{g}_R \boldsymbol{B}$ in the two dots differ significantly, and their energy scales $|\mu_B \hat{g}_L \boldsymbol{B}|$ and $|\mu_B \hat{g}_R \boldsymbol{B}|$ are comparable to the interdot tunnel amplitude t; these conditions ensure efficient singlet-triplet mixing[31] and a large current as seen in Fig. 3a. If the magnetic field is oriented along the same direction, but decreased in magnitude, $|\mu_B \hat{g}_{L,R} \boldsymbol{B}| \ll t$, then the hybridized singlet states with energies around $\pm\sqrt{2}t$ are hardly mixed with the triplets around zero energy, hence the latter ones block transport and the current decreases, as seen in Fig. 3a.

To conclude, we characterized the ultimate sensitivity of a directionally sensitive magnetometry scheme, where the sharp, magnetic-field-induced variations of the current through a Pauli-blockaded DQD are used to measure small changes of the external magnetic field. Using parameter values taken from CNT DQD experiments, we estimate that the sensitivity of such a device can reach a few tens of nT/$\sqrt{\rm Hz}$.

V. DISCUSSION

A. The role of the temperature

Based on Eq. (2), we argued that the optimal sensitivity of the Coulomb-blockade magnetometer is degraded if the temperature is increased. On the other hand, the sensitivity of a Pauli-blockade magnetometer is not influenced directly by the temperature, see Eq. (7). The only requirement on temperature for the Pauli-blockade magnetometry scheme to work is that the orbital level spacing of the dots should dominate the thermal energy scale. One remarkable consequence of this fact is that downsizing the proposed Pauli-blockade magnetometry scheme, e.g., using an atom-sized DQD based on small donor ensembles,[37,38] which would provide larger orbital level spacings, should allow for a higher temperature of operation. Such a miniaturization would provide an added benefit: enhanced spatial resolution.

B. Optimal sensitivity and dynamical range for the Pauli-blockade magnetometer

The optimal value of the sensitivity in Fig. 3d is $S_{\rm opt} = 37$ nT/$\sqrt{\rm Hz}$, at the point $(B_{0z}, B_{0x}) = (0, 25)$ mT. However, this is not a suitable working point if we want to use the device as a linear detector of δB_z, since the dependence of the current on δB_z is quadratic here, see Eq. 5 and Fig. 3b. In other words, even though the sensitivity is optimal at this working point, the dynamical range of the device as a linear detector of δB_z is zero. Therefore, in practice, the achievable optimal sensitivity is slightly degraded with respect to $S_{\rm opt}$, and depends

on the desired dynamical range. For example, according to Figs. 3b,d, choosing the working point around $(B_{0z}, B_{0x}) = (0.25, 100)\,\mathrm{mT}$, results in a dynamical range of a few hundred microteslas and a sensitivity around $50\,\mathrm{nT}/\sqrt{\mathrm{Hz}}$.

C. The role of electric potential fluctuations

Electric potential fluctuations might arise from, e.g., gate voltage noise or the randomly varying occupation of charge traps near the dots. These fluctuations detune the dots' energy levels from their pre-defined positions. On the one hand, this has a direct influence on the sensitivity of the Coulomb-blockade magnetometry scheme presented in Sec. III, since the noise-induced detuning competes with the magnetic energy shift which one wants to measure. On the other hand, our perturbative result (4) suggest that the Pauli-blockade magnetometry enjoys some protection against electrical potential fluctuations: the overlap (4) and hence the decay rate $\bar{\Gamma} = 2\Gamma_R \left|\langle S_g|\bar{T}_0\rangle\right|^2$ of $\bar{T}_0$ are independent of the (1,1)-(0,2) energy detuning Δ. Therefore, even if a weak noise induces fluctuations of Δ, the decay rate $\bar{\Gamma}$ and hence the characteristics of current flow through the device remain unchanged, and the sensitivity of the magnetometer will not be degraded. We also note that the alternative Coulomb-blockade magnetometry scheme, corresponding to the vicinity of the working point □ in Fig. 2d, also enjoys protection against electrical potential fluctuations; see Appendix B for a discussion.

D. Different g factors in the two dots

In section IV, we considered a model of a DQD where the principal values $g_\parallel$ and $g_\perp$ of the g-tensors are identical in the two dots. Within this model, the two key qualitative results we have emphasized were the following. (i) If the homogeneous magnetic field $\boldsymbol{B}_0$ is oriented along x, then the T_0 blockade sets in, and the dependence of the current on the component of the magnetic field that is in the xz plane and perpendicular to $\boldsymbol{B}_0$ allows the measurement of the latter. (ii) The independence of the decay rate $\bar{\Gamma}$ from the detuning Δ indicates that the magnetic-field sensitivity of the Pauli-blockade magnetometry is robust against electric potential fluctuations. We emphasize that these two results are not restricted to the case when $g_\perp$ and $g_\parallel$ are identical in the two dots; if the g tensors are more generic, but still allow for the T_0 blockade to appear, then both properties (i) and (ii) remain. The generic condition for the T_0 blockade is that the local effective magnetic fields on the two dots should have the same absolute values:[31] $|\hat{\mathbf{g}}_L\boldsymbol{B}| = |\hat{\mathbf{g}}_R\boldsymbol{B}|$. If such a magnetic-field orientation exists for the given g-tensors, and the field is oriented along that direction, then a a single (1,1) two-electron triplet state is decoupled from the others and blocks the current. If we take the spin quantization axis along $\hat{\mathbf{g}}_L\boldsymbol{B} + \hat{\mathbf{g}}_L\boldsymbol{B}$, then this blocking state is in fact $T_0 = \frac{1}{\sqrt{2}}(\uparrow\downarrow + \downarrow\uparrow)$.

E. Mechanical stability requirement for the Pauli-blockade magnetometer

If the particular realization of the Pauli-blockade magnetometry discussed here is used as a scanning probe, then an important requirement is the mechanical stability of the setup. This requirement is related to the fact that in the Pauli-blockade magnetometry setup, the measured quantity (current) is sensitive to a magnetic-field component that is perpendicular to the offset field. Recall that in the Pauli-blockade magnetometry, a homogeneous external magnetic field (offset field) is applied, which is almost aligned with the x axis of the reference frame; for example, $\boldsymbol{B}_0 = (100, 0, 0.25)$ mT. Then, measuring the current provides a measurement of δB_z, that is, the z component of the unknown part of the magnetic field. However, in the presence of weak mechanical noise, influencing either the offset field direction or the DQD orientation, their enclosed angle will change. For example, consider the change when, due to some mechanical instability, the offset field suffers an unwanted rotation $\boldsymbol{B}_0 \mapsto \boldsymbol{B}_0'$ around the y axis with a small angle $\beta = 1/50 \approx 1$ degree. This change will give rise to an offset-field z component $B_{0z}' \approx B_{0x}\sin\beta \approx 2$ mT, far exceeding the original working-point value $B_{0z} = 0.25$ mT. This observation highlights the requirement of a high degree of mechanical stability in potential future devices realizing the proposed magnetometry scheme.

F. Realization

The key elements of the schemes studied here have already been realized in CNT-based quantum dot systems, suggesting the feasibility of the outlined principles. Note that the spin degree of freedom in the models used in this work correspond to the combined spin-valley states in CNTs that form twofold degenerate Kramers doublets in the absence of a magnetic field.[27]

High-quality single and double dots,[25–27,39–44] including those in bent CNTs,[34,36,45,46] have been fabricated. Longitudinal g-factors up to $g_\parallel \approx 50$ have been measured,[26] and Pauli blockade was observed.[34,36,39,40] Part of the experimental data in a bent-CNT DQD (see Fig. S7 in the Supplementary Information of Ref. 34) and its comparison with theory (see Fig. 1c in Ref. 35) suggest that in that device, the g-tensors show the characteristics required to realize the scheme proposed here, and that the T_0 blockade (referred to as 'antiresonance' in Ref. 35) have already been observed.

Scanning-probe devices based on quantum dots,[47] including a gate-tunable CNT quantum dot,[48] have already

been fabricated and used for imaging electric fields. Besides demonstrating that CNT dots are compatible with scanning-probe technology, the latter fact also highlights the opportunity to use quantum dots as hybrid sensors, with in situ switching capability between electric-field and magnetic-field sensing.

Nuclear spins can provide a strong magnetic noise for the electron spins via the hyperfine interaction, and therefore their presenence is expected to degrade the performance of the magnetometer setups described in this work. This effect might be detrimental for magnetic-field sensing with dots in frequenty used III-V semiconductor hosts, such as GaAs, InAs or InSb, where the strength of the hyperfine-induced magnetic noise is in the millitesla range.[30] In contrast, CNTs have the advantage of a low, 1% abundance of nuclear spins, which can be further lowered using isotopic purification, mitigating the harmful effect of the nuclear-spin bath.

VI. CONCLUSIONS

We have presented two magnetic-field sensing principles, which are based on electron transport in Coulomb- and Pauli-blockaded quantum dots. We demonstrated that the fundamental limit of the magnetic-field sensitivity in such devices can be below $\mu\mathrm{T}/\sqrt{\mathrm{Hz}}$. A carbon nanotube might be optimal as a host material. Downsizing the proposed scheme, e.g., using an atomic-sized double quantum dot based on small donor ensembles, might lead to further improved spatial resolution, and, as a consequence of higher orbital level spacings, a broader temperature range of operation.

ACKNOWLEDGMENTS

We thank K. Nowack and Sz. Csonka for useful discussions. We acknowledge funding from the EU Marie Curie Career Integration Grant CIG-293834 (CarbonQubits), the OTKA Grant PD 100373, the OTKA Grant 108676, and the EU ERC Starting Grant CooPairEnt 258789. A. P. is supported by the János Bolyai Scholarship of the Hungarian Academy of Sciences.

Appendix A: Derivation of the sensitivity formula

Here we show that the shot-noise-limited magnetic-field sensitivity of a current-based magnetometer is characterized by Eq. (1). The notation used here follows that introduced in the main text.

Charge flow through the device has a random character, since electron tunneling between the leads and the conductor occur in a random fashion. To describe this randomness, we use $P(N,\tau)$, the probability that in the time window between $t=0$ and $t=\tau$, the number of electrons entering the drain contact is N. The normalization condition is that $\sum_{N\in\mathbb{Z}} P(N,\tau)=1$ for any τ. Henceforth we assume that the device is in its steady state, and that $P(N,\tau)$ corresponds to this steady state.

We assume that the current is measured by counting the electrons entering the drain during the measurement time window $t\in[0,\tau]$. The number of transmitted electrons is a random variable; let us characterize its probability distribution by its average $\mathcal{N}(\tau)=\sum_{N\in\mathbb{Z}} NP(N,\tau)$ and its variance $\sigma^2(\tau)=\sum_{N\in\mathbb{Z}}[N-\mathcal{N}(\tau)]^2 P(N,\tau)$. Note that in the steady state, both quantities are proportional to the measurement time τ (see Refs. 28 and 29 and Eqs. (C4) and (C5) below), which motivates the definitions of the electric current I and the Fano factor F,

$$I=-e\mathcal{N}(\tau)/\tau, \tag{A1}$$

$$F=\sigma^2(\tau)/\mathcal{N}(\tau), \tag{A2}$$

which are τ-independent quantities. Here, e denotes the absolute value of the electron charge.

In the considered generic magnetometer, both the average and the variance depend on the magnetic field, $\mathcal{N}(\tau)=\mathcal{N}(\tau,B)$ and $\sigma^2(\tau)=\sigma^2(\tau,B)$. The task is the following. Assume that $I(B)$ is known, and that a known working-point magnetic field B_0 is switched on. There is also an unknown small component δB of the magnetic field $B=B_0+\delta B$. We wish to determine δB by measuring the number of electrons entering the drain contact in a given measurement time window τ. That is possible, if the change of the average number of transmitted electrons induced by δB exceeds the standard deviation of the transmitted electrons at the working point. This condition is formalized as

$$|\mathcal{N}(\tau,B_0+\delta B)-\mathcal{N}(\tau,B_0)|>\sigma(\tau,B_0). \tag{A3}$$

This condition leads to a natural definition of the magnetic-field sensitivity in accordance with Eq. (1): After (i) linearizing Eq. (A3) in δB, (ii) expressing the resulting formula in terms of the current I and Fano factor F defined in Eqs. (A1) and (A2), and (iii) rearranging the two sides of the resulting equation, we find that the minimal change in magnetic field that can be resolved by the current measurement is constrained by

$$|\delta B|>\frac{1}{\sqrt{\tau}}\frac{\sqrt{eF(B_0)I(B_0)}}{|I'(B_0)|} \tag{A4}$$

where the prime denotes the derivative with respect to the magnetic field.

We conclude that the second fraction on the right hand side of Eq. (A4), defined as the magnetic-field sensitivity S in Eq. (1), does indeed characterize the performance of the magnetometer: for a given measurement time τ, the minimum resolvable change in the magnetic field is $S/\sqrt{\tau}$.

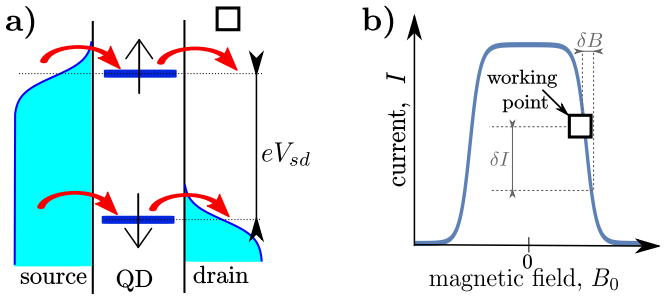

FIG. 4. Alternative operation of a Coulomb-blockade magnetometer. (a) Level diagram corresponding to the optimal-sensitivity working point marked by □ in Fig. 2c. Here, the offset magnetic field and the source-drain bias are chosen so that the two spin levels are aligned with the chemical potentials of the two leads. (b) Magnetic-field dependence of the current in the vicinity of the working point □. The width of the current plateau is $\sim eV_{sd}/g\mu_B$, that is, it is set by the source-drain bias V_{sd}. The width of the slopes connecting the zero-current range with the current plateau is $\sim k_BT/g\mu_B$, that is, it is set by the temperature T.

Appendix B: An alternative scheme of Coulomb-blockade magnetometry

In Fig. 2d, the global minimum of the magnetic-field sensitivity S is at the point marked by the white square □, that is, at $(\epsilon, B_0) \approx (0\,\mu\text{eV}, 10\,\text{mT})$. As mentioned in section III, the operation of the magnetometer at this working point does not follow the scheme proposed there: the level alignment is not as shown in Fig. 1b. We show the schematic level alignment for the working point □ in Fig. 4a: each Zeeman-split level is located in the vicinity of the chemical potential of one of the leads. In this situation, the dependence of the current on the magnetic field is due to the following reason. A small change $\delta B > 0$ in the magnetic field shifts the energy of the $\downarrow$ ($\uparrow$) state downwards (upwards), therefore the outgoing (incoming) rate towards the drain (from the source) decreases. That is, transport through both levels is suppressed, and therefore the current decreases, as shown schematically in Fig. 4b.

We expect that the effect of electrical potential fluctuations, that is, the effect of the noise of the on-site energy ϵ, can be mitigated by choosing a special working point in the vicinity of □. We illustrate this opportunity using Fig. 5. Figure 5a shows the current as a function of the magnetic field B_0 and the on-site energy ϵ, whereas Fig. 5b shows the derivative of the current with respect to the on-site energy, $\frac{\partial I}{\partial \epsilon}$. A strongly reduced effect of ϵ-noise on the magnetic-field sensitivity is expected in the working points along the contour where $\frac{\partial I}{\partial \epsilon} = 0$ (see Fig. 5b). In order to simultaneously exploit the opportunity for charge-noise resilience and obtain a good magnetic-field sensitivity S, one should find the minimum of S along the $\frac{\partial I}{\partial \epsilon} = 0$ contour. The resulting optimal working point is denoted with the black star in Fig. 5c, where the sensitivity is shown together with the $\frac{\partial I}{\partial \epsilon} = 0$ contour (solid blue line). The sensitivity corresponding to this optimal working point is $S_{\text{opt}} \approx 2\,\mu\text{T}/\sqrt{\text{Hz}}$.

Appendix C: Calculating current and shot noise using rate equations

Here, we present the counting-field method[28,29] we used to calculate the current and the shot noise of the considered setups, and outline the derivation of the specific results for the Coulomb-blockade and Pauli-blockade magnetometers.

1. Generic framework to calculate the current and the shot noise: the counting-field method

The transport process consists of single-electron tunneling events between the source and the conductor and between the conductor and the drain. Electrons in the conductor can occupy M different states; for example, in the Coulomb-blockade magnetometer setup we consider in section III we have $M = 3$, as there are three electronic states involved in the transport cycle: the empty dot, and the two Zeeman-split single-electron states $\downarrow$ and $\uparrow$. We assume that the number of charges arriving to the drain is being measured from some initial point $t = 0$ in time. Then, the random character of the tunneling events is described by the probability density function $P_i(N,\tau)$ where $i = 1,\ldots,M$; $N \in \mathbb{Z}$; $\tau > 0$: this is the probability of that at time τ, the conductor is in its $i$the electronic state, and N electrons have arrived to the drain since $t = 0$. Note that the relation between the probability $P_j(N,\tau)$ introduced here and the probability $P(N,\tau)$ introduced in section A is simply $P(N,\tau) = \sum_{i=1}^{M} P_i(N,\tau)$. The normalization condition reads $\sum_{i=1}^{M}\sum_{N\in\mathbb{Z}} P_i(N,\tau) = 1$ for all τ. We introduce the vector $\mathbf{P}(N,\tau) = (P_1(N,\tau),\ldots,P_M(N,\tau))$. The time evolution of $\mathbf{P}(N,\tau)$ is governed by a rate equation and depends on the initial (in general, mixed) electronic state characterized by $\mathbf{P}(0,0)$. However, here we focus only on the steady-state current and shot noise, and disregard transient effects.

The effect of random single-electron tunneling events is described by the following rate equation:

$$\partial_\tau \mathbf{P}(N,\tau) = \mathbf{\Gamma}_0\mathbf{P}(N,\tau) + \boldsymbol{J}^+\mathbf{P}(N-1,\tau) + \boldsymbol{J}^-\mathbf{P}(N+1,\tau), \tag{C1}$$

where the rate matrices $\mathbf{\Gamma}_0$, $\boldsymbol{J}^+$ and $\boldsymbol{J}^-$ have size $M\times M$. The matrix $\boldsymbol{J}^+$ ($\boldsymbol{J}^-$) represents single-electron tunneling events from the conductor to the drain (from the drain to the conductor). For a concrete example for such a rate equation, see Eq. (C6), the one for the Coulomb-blockade magnetometer.

As the rate matrices are independent of N, the infinite coupled set (C1) of differential equations can be partially

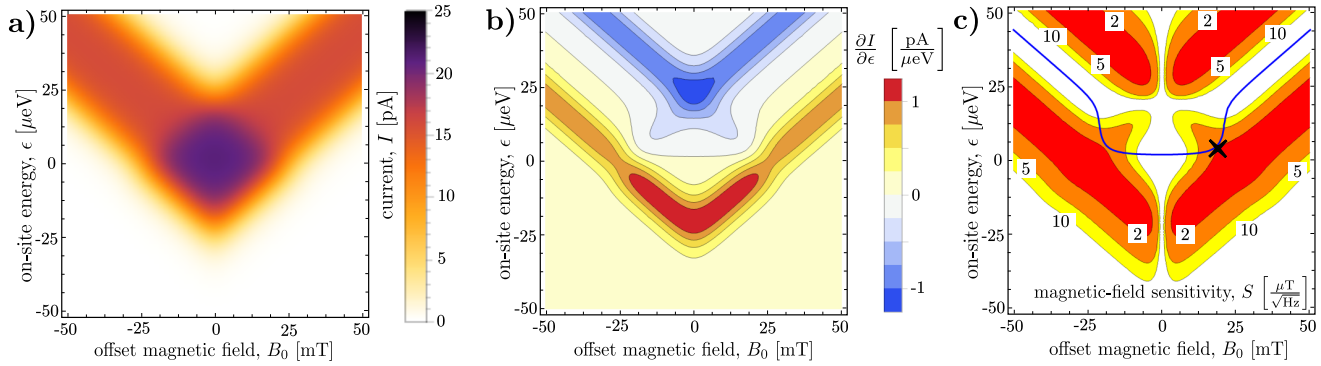

FIG. 5. Charge-noise-resilient working point of the Coulomb-blockade magnetometer. (a) Current $I(B_0, \epsilon)$ as a function of the magnetic field and the quantum dot on-site energy. (b) Derivative of the current with respect to the on-site energy. Working points along the contour $\frac{\partial I}{\partial \epsilon} = 0$ are expected to have a reduced susceptibility to charge noise (i.e., fluctuations of ϵ). (c) Magnetic-field sensitivity $S(B_0, \epsilon)$. The solid blue line is the $\frac{\partial I}{\partial \epsilon} = 0$ contour. The black star is the working point where the magnetic-field sensitivity is optimized ($S_{\text{opt}} \approx 2\,\mu\text{T}/\sqrt{\text{Hz}}$) along the contour. Parameters: same as in Fig. 2, except that $V_{sd} = 43\,\mu\text{V}$.

decoupled with the following Fourier transformation:

$$\tilde{\mathbf{P}}(\chi, \tau) = \sum_{N \in \mathbb{Z}} \mathbf{P}(N, \tau)\, e^{iN\chi}, \tag{C2}$$

where $\chi \in]-\pi, \pi]$. Acting on Eq. (C1) with this Fourier transformation yields

$$\partial_\tau \tilde{\mathbf{P}}(\chi, \tau) = (\mathbf{\Gamma}_0 + \boldsymbol{J}^+ e^{i\chi} + \boldsymbol{J}^- e^{-i\chi})\tilde{\mathbf{P}}(\chi, \tau) = \boldsymbol{M}(\chi)\tilde{\mathbf{P}}(\chi, \tau). \tag{C3}$$

Here the second equality is the definition of $\boldsymbol{M}(\chi)$, and χ is referred to as the *counting field*. For every value of χ, Eq. (C3) represents a coupled set of M differential equations.

As shown in Refs. 28 and 29, the steady-state current and the steady-state shot noise are both related to the eigenvalue branch $\lambda_1(\chi)$ of $\boldsymbol{M}(\chi)$ that fulfills $\lambda_1(\chi = 0) = 0$. The average number of transmitted electrons in the steady state is

$$\mathcal{N}(\tau) = \sum_{N \in \mathbb{Z}} N P(N, \tau) = -i\,\tau \frac{\partial \lambda_1(\chi)}{\partial \chi}\bigg|_{\chi=0}, \tag{C4}$$

whereas the variance is

$$\sigma^2(\tau) = \sum_{N \in \mathbb{Z}} \left[N^2 - \mathcal{N}^2(\tau)\right] P(N, \tau) = -\,\tau \frac{\partial^2 \lambda_1(\chi)}{\partial \chi^2}\bigg|_{\chi=0}. \tag{C5}$$

These equations are then used to express the current via Eq. (A1) and the Fano factor via Eq. (A2). To obtain the numerical results shown in Figs. 2 and 3, we have numerically evaluated the first and second derivatives of $\lambda_1(\chi)$ after numerical diagonalization of the matrix $\boldsymbol{M}(\chi)$ at $\chi = 0$ and $\chi = \pm 10^{-5}$.

2. Rate equation for the Coulomb-blockade magnetometer

The rate equation describing electron transport through the Coulomb-blockade magnetometer, i.e., a single quantum dot, reads:

$$\begin{aligned}
\dot{P}_\sigma(N, \tau) = &-\sum_s \Gamma^{\text{out}}_{\sigma,s} P_\sigma(N, \tau) + \Gamma^{\text{in}}_{\sigma,L} P_0(N, \tau) + \\
&+ \Gamma^{\text{in}}_{\sigma,R} P_0(N+1, \tau), \\
\dot{P}_0(N, \tau) = &\sum_\sigma \Gamma^{\text{out}}_{\sigma,R} P_\sigma(N-1, \tau) + \sum_\sigma \Gamma^{\text{out}}_{\sigma,L} P_\sigma(N, \tau) - \\
&- \sum_{\sigma,s} \Gamma^{\text{in}}_{\sigma,s} P_0(N, \tau),
\end{aligned} \tag{C6}$$

where $\sigma \in \{\downarrow = -1, \uparrow = +1\}$ and the indices of the leads are $s \in \{L, R\}$. Here, $P_0(N, \tau)$ is the joint probability of the event that the dot is empty at time τ and N electrons have entered the drain between $t = 0$ and $t = \tau$. Similarly, $P_\uparrow(N, \tau)$ [$P_\downarrow(N, \tau)$] is the joint probability of the event that the dot is occupied with a spin-up [spin-down] electron at time τ, and N electrons have entered the drain between $t = 0$ and $t = \tau$. Furthermore, the transition rates $\Gamma^{\text{in}}_{\sigma,s} = \Gamma f_{\text{FD}}(\epsilon_\sigma - \mu_s)$ and $\Gamma^{\text{out}}_{\sigma,s} = \Gamma\,(1 - f_{\text{FD}}(\epsilon_\sigma - \mu_s))$ are expressed using the lead-dot tunnelling rate Γ and the Fermi-Dirac distribution $f_{\text{FD}}(x) = \frac{1}{e^{x/(k_B T)}+1}$. The chemical potentials are biased symmetrically $\mu_L = -\mu_R = \frac{eV_{sd}}{2}$. Due to the Zeeman splitting, the spin-dependent energy of the single occupied dot is $\epsilon_\sigma = \epsilon + \frac{1}{2}\sigma g \mu_B B$.

Using this rate equation, we apply the counting-field method outlined above to calculate the current and the Fano factor. We used analytical results for the current to generate Figs. 2a,b and 5a, 5b. The Fano factor shown in 2c, as well as the sensitivities shown in Figs. 2d and 5c, are evaluated numerically.

3. Rate equation for the Pauli-blockade magnetometer

Here, we present the rate equation we use to describe the transport process through the considered Pauli-blockaded double quantum dot. The rates of $(0,1) \to (1,1)$ $[(0,2) \to (0,1)]$ transitions are parametrized by the rate Γ_L $[\Gamma_R]$, describing single-electron tunneling from the source to the left dot [from the right dot to the drain]. These considerations result in the following classical master equation:[49]

$$\dot{P}_j(N,\tau) = -2\Gamma_R v_j P_j(N,\tau) + \frac{1}{2}\Gamma_{\rm L}(1-v_j)P_6(N,\tau),$$
$$\dot{P}_6(N,\tau) = -2\Gamma_{\rm L} P_6(N,\tau) + 2\Gamma_R \sum_{j=1}^{5} v_j P_j(N-1,\tau). \quad \text{(C7)}$$

Here, $P_j(N,\tau)$ with $j \in \{1,2,3,4,5\}$ is the joint probability of the event that the j-th two-electron energy eigenstate Ψ_j of the double-dot Hamiltonian $H = H_B + H_{\rm tun} + H_\Delta$ (see main text) is occupied at time τ and N electrons have entered the drain between $t = 0$ and $t = \tau$. Similarly, $P_6(N,\tau)$ is the joint probability of the event that a (0,1) state is occupied, and N electrons have entered the drain between $t = 0$ and $t = \tau$. Furthermore, v_j $[1 - v_j]$ is the weight of the two-electron energy eigenstate Ψ_j in the (0,2) [(1,1)] charge configuration, that is, $v_j = |\langle \Psi_j | S_g \rangle|^2$; note that $\sum_{j=1}^{5} v_j = 1$.

4. Perturbative analytical results for the current and the shot noise in the vicinity of T_0 blockade

In the description of the Pauli-blockade magnetometer in section IV, we quote analytical results for the electrical current, Eq. 5, and the Fano factor, Eq. 6. These results are valid in the case when B_z is sufficiently small, that is, when the decay rate $\bar{\Gamma}$ of the state $\bar{T}_0$ is much smaller than any other transition rate in the rate equation (C7). To arrive to these analytical results, we use the perturbative technique applied in Ref. 29. The key steps are: (i) The size of $\boldsymbol{M}(\chi)$ is 6×6, hence the characteristic polynomial of $\boldsymbol{M}(\chi)$ is of sixth order, $C(\lambda,\bar{\Gamma}) = \sum_{i=1}^{6} c_i(\bar{\Gamma})\lambda^i$; here the coefficients $c_i(\bar{\Gamma})$ are explicitly determined by the matrix elements of $\boldsymbol{M}(\chi)$. (ii) For $\bar{\Gamma} = 0$, the state T_0 is the steady state, with the corresponding eigenvalue $\lambda_1(\bar{\Gamma} = 0) = 0$. (iii) For small but nonzero $\bar{\Gamma}$, the eigenvalue λ_1 developing from $\lambda_1(\bar{\Gamma} = 0) = 0$ is assumed to be linear in $\bar{\Gamma}$, that is, of the form $\lambda_1 = \alpha\bar{\Gamma}$. (iv) Substituting $\lambda = \alpha\bar{\Gamma}$ to the characteristic polynomial $C(\lambda,\bar{\Gamma})$, first-order Taylor-expanding the latter in $\bar{\Gamma}$, and equating the result to zero, yields the linear equation

$$C(\lambda,\bar{\Gamma}) \approx \left.\frac{dc_0(\bar{\Gamma})}{d\bar{\Gamma}}\right|_{\bar{\Gamma}=0} \bar{\Gamma} + c_1(0)\alpha\bar{\Gamma} = 0. \quad \text{(C8)}$$

Solving this for α yields

$$\lambda_1(\chi) = \alpha\bar{\Gamma} = -\frac{\left.\frac{dc_0(\bar{\Gamma})}{d\bar{\Gamma}}\right|_{\bar{\Gamma}=0}}{c_1(0)}\bar{\Gamma} = -4\bar{\Gamma}\frac{1-e^{i\chi}}{4-3e^{i\chi}}. \quad \text{(C9)}$$

This result was used, together with Eqs. (C4) and (C5) to obtain the results for the current and the Fano factor.

Appendix D: Resilience to charge noise: detuning-independent decay rate of $\bar{T}_0$

Here we provide the derivation of Eq. (4) of the main text. As stated there, we use first-order perturbation theory to arrive to the result. Nevertheless, we do present the derivation here as it involves one nontrivial technical step: Usually, the application of perturbation theory is based on the knowledge of the eigensystem of the unperturbed Hamiltonian; we do not have that knowledge here, which necessitates an alternative approach to arrive to the result.

We start by evaluating the two-electron Hamiltonian $H = H_B + H_{\rm tun} + H_\Delta$ (see main text) exactly at the T_0 blockade, that is, at $\boldsymbol{B} = (B,0,0)$. We set the spin quantization axis along x, and express H in the basis T_+, T_-, S, S_g, T_0; the corresponding matrix reads[31,35,50]

$$H_0 = \left(\begin{array}{cccc|c} \mathcal{B}_s & 0 & -\mathcal{B}_{a\perp}/\sqrt{2} & 0 & 0 \\ 0 & -\mathcal{B}_s & \mathcal{B}_{a\perp}/\sqrt{2} & 0 & 0 \\ -\mathcal{B}_{a\perp}/\sqrt{2} & \mathcal{B}_{a\perp}/\sqrt{2} & 0 & \sqrt{2}t & 0 \\ 0 & 0 & \sqrt{2}t & -\Delta & 0 \\ \hline 0 & 0 & 0 & 0 & 0 \end{array}\right) \quad \text{(D1)}$$

where $\mathcal{B}_s = \frac{1}{2}\mu_B\left[(\hat{\boldsymbol{g}}_L + \hat{\boldsymbol{g}}_R)\boldsymbol{B}\right]_x$ and $\mathcal{B}_{a\perp} = \frac{1}{2}\mu_B[(\hat{\boldsymbol{g}}_L - \hat{\boldsymbol{g}}_R)\boldsymbol{B}]_z$. The upper left 4×4 block of H_0 will be referred to as H_0'. In H_0, the unpolarized triplet T_0 is decoupled from the other states and therefore blocks the current. A finite magnetic-field component along z, entering the Hamiltonian as a perturbation $H_1 = \mathcal{B}_{a\parallel}(|T_0\rangle\langle S| + h.c.)$, mixes T_0 with the other states. Here $\mathcal{B}_{a\parallel} = \frac{1}{2}\mu_B[(\hat{\boldsymbol{g}}_L - \hat{\boldsymbol{g}}_R)\boldsymbol{B}]_x$, and we will denote the perturbed T_0 state by $\bar{T}_0$.

We were unable to find analytical expressions for the eigensystem of H_0', which would have provided a convenient starting point for doing perturbation theory in H_1. However, the overlap $\langle S_g|\bar{T}_0\rangle$ we are looking for, which determines the decay rate of the blocking state $\bar{T}_0$, can be expressed in an alternative way. Start with the standard first-order perturbative formula for the energy eigenstates:

$$\langle S_g|\bar{T}_0\rangle = \langle S_g|\left[|T_0\rangle + \sum_{i=1}^{4}\frac{|i\rangle\langle i|H_1|T_0\rangle}{E(T_0)-E(i)}\right]$$
$$= -\mathcal{B}_{a\parallel}\langle S_g|(H_0')^{-1}|S\rangle. \quad \text{(D2)}$$

Here, $|i\rangle$ and $E(i)$ $(i \in \{1,2,3,4,T_0\})$ are the eigenstates and eigenvalues of H_0, respectively. In the second step, we used the form of H_1 given above, the value $E(T_0) = 0$,

and the fact that $\sum_{i=1}^{4} \frac{|i\rangle\langle i|}{E(i)} = (H_0')^{-1}$. The 4×4 matrix H_0' can be inverted analytically, yielding $\langle S_g|\bar{T}_0\rangle = -\frac{\mathcal{B}_{a\|}}{\sqrt{2}t}$. Importantly, this result is independent of the (1,1)-(0,2) energy detuning Δ, which is apparent from the above definition of $\mathcal{B}_{a\|}$; this Δ-independence provides the feature of charge-noise-resilience of the proposed magnetometer, discussed in Sec. V C. Using the conditions $B_z \ll B_x$, $\alpha \ll 1$, and $g_\perp \ll g_\|$, fulfilled by the realistic parameter set used in the main text, we find $\mathcal{B}_{a\|} \approx \mu_B B_z \alpha \frac{g_\|^2}{g_\perp}$, leading to the result (4).

[1] S. J. Bending, Advances in Physics **48**, 449 (1999).
[2] Y. Martin and H. K. Wickramasinghe, Applied Physics Letters **50**, 1455 (1987).
[3] A. M. Chang, H. D. Hallen, L. Harriott, H. F. Hess, H. L. Kao, J. Kwo, R. E. Miller, R. Wolfe, J. van der Ziel, and T. Y. Chang, Applied Physics Letters **61**, 1974 (1992).
[4] J. R. Kirtley, M. B. Ketchen, K. G. Stawiasz, J. Z. Sun, W. J. Gallagher, S. H. Blanton, and S. J. Wind, Applied Physics Letters **66**, 1138 (1995).
[5] J. C. Allred, R. N. Lyman, T. W. Kornack, and M. V. Romalis, Phys. Rev. Lett. **89**, 130801 (2002).
[6] D. Rugar, R. Budakian, H. J. Mamin, and B. W. Chui, Nature **430**, 329 (2004).
[7] J. M. Taylor, P. Cappellaro, L. Childress, L. Jiang, D. Budker, P. R. Hemmer, A. Yacoby, R. Walsworth, and M. D. Lukin, Nat Phys **4**, 810 (2008).
[8] P. Milde, D. Khler, J. Seidel, L. M. Eng, A. Bauer, A. Chacon, J. Kindervater, S. Mhlbauer, C. Pfleiderer, S. Buhrandt, C. Schtte, and A. Rosch, Science **340**, 1076 (2013).
[9] M. Switkes, A. G. Huibers, C. M. Marcus, K. Campman, and A. C. Gossard, Applied Physics Letters **72**, 471 (1998).
[10] B. Lassagne, D. Ugnati, and M. Respaud, Phys. Rev. Lett. **107**, 130801 (2011).
[11] J. R. Kirtley, C. C. Tsuei, M. Rupp, J. Z. Sun, L. S. Yu-Jahnes, A. Gupta, M. B. Ketchen, K. A. Moler, and M. Bhushan, Phys. Rev. Lett. **76**, 1336 (1996).
[12] M. Pelliccione, A. Jenkins, P. Ovartchaiyapong, C. Reetz, E. Emmanuelidu, N. Ni, and A. C. B. Jayich, ArXiv:1510.02780 (unpublished).
[13] L. Thiel, D. Rohner, M. Ganzhorn, P. Appel, E. Neu, B. Muller, R. Kleiner, D. Koelle, and P. Maletinsky, ArXiv:1511.02873 (unpublished).
[14] I. Kezsmarki, S. Bordacs, P. Milde, E. Neuber, L. M. Eng, J. S. White, H. M. Ronnow, C. D. Dewhurst, M. Mochizuki, K. Yanai, H. Nakamura, D. Ehlers, V. Tsurkan, and A. Loidl, Nat Mater **14**, 1116 (2015).
[15] X. R. Wang, C. J. Li, W. M. L, T. R. Paudel, D. P. Leusink, M. Hoek, N. Poccia, A. Vailionis, T. Venkatesan, J. M. D. Coey, E. Y. Tsymbal, Ariando, and H. Hilgenkamp, Science **349**, 716 (2015).
[16] H. Bluhm, N. C. Koshnick, J. A. Bert, M. E. Huber, and K. A. Moler, Phys. Rev. Lett. **102**, 136802 (2009).
[17] B. Kalisky, E. M. Spanton, H. Noad, J. R. Kirtley, K. C. Nowack, C. Bell, H. K. Sato, M. Hosoda, Y. Xie, Y. Hikita, C. Woltmann, G. Pfanzelt, R. Jany, C. Richter, H. Y. Hwang, J. Mannhart, and K. A. Moler, Nat. Mater. **12**, 1091 (2013).
[18] E. M. Spanton, K. C. Nowack, L. Du, G. Sullivan, R.-R. Du, and K. A. Moler, Phys. Rev. Lett. **113**, 026804 (2014).
[19] K. C. Nowack, E. M. Spanton, M. Baenninger, M. König, J. R. Kirtley, B. Kalisky, C. Ames, P. Leubner, C. Brüne, H. Buhmann, L. W. Molenkamp, D. Goldhaber-Gordon, and K. A. Moler, Nat Mater **12**, 787 (2013).
[20] K. Ono, D. G. Austing, Y. Tokura, and S. Tarucha, Science **297**, 1313 (2002).
[21] A. N. Korotkov, D. V. Averin, K. K. Likharev, and S. A. Vasenko, in *Single-Electron Tunneling and Mesoscopic Devices* (Springer-Verlag Berlin Heidelberg 1992, 1992).
[22] Y. Blanter and M. Büttiker, Physics Reports **336**, 1 (2000).
[23] A. N. Korotkov, Phys. Rev. B **49**, 10381 (1994).
[24] H. Ajiki and T. Ando, Journal of the Physical Society of Japan **62**, 1255 (1993).
[25] E. D. Minot, Y. Yaish, V. Sazonova, and P. L. McEuen, Nature **428**, 536 (2004).
[26] F. Kuemmeth, S. Ilani, D. C. Ralph, and P. L. McEuen, Nature **452**, 448 (2008).
[27] E. A. Laird, F. Kuemmeth, G. A. Steele, K. Grove-Rasmussen, J. Nygård, K. Flensberg, and L. P. Kouwenhoven, Rev. Mod. Phys. **87**, 703 (2015).
[28] D. A. Bagrets and Y. V. Nazarov, Phys. Rev. B **67**, 085316 (2003).
[29] W. Belzig, Phys. Rev. B **71**, 161301 (2005).
[30] F. H. L. Koppens, J. A. Folk, J. M. Elzerman, R. Hanson, L. H. W. van Beveren, T. Vink, H. P. Tranitz, W. Wegscheider, L. P. Kouwenhoven, and L. M. K. Vandersypen, Science **309**, 1346 (2005).
[31] O. N. Jouravlev and Y. V. Nazarov, Phys. Rev. Lett. **96**, 176804 (2006).
[32] A. Pfund, I. Shorubalko, K. Ensslin, and R. Leturcq, Phys. Rev. Lett. **99**, 036801 (2007).
[33] J. Danon and Y. V. Nazarov, Phys. Rev. B **80**, 041301 (2009).
[34] F. Pei, E. A. Laird, G. A. Steele, and L. P. Kouwenhoven, Nat. Nanotech. **7**, 630 (2012).
[35] G. Széchenyi and A. Pályi, Phys. Rev. B **91**, 045431 (2015).
[36] E. A. Laird, F. Pei, and L. P. Kouwenhoven, Nat. Nanotech. **8**, 565 (2013).
[37] B. Weber, S. Mahapatra, T. F. Watson, and M. Y. Simmons, Nano Letters **12**, 4001 (2012).
[38] B. Weber, Y. H. M. Tan, S. Mahapatra, T. F. Watson, H. Ryu, R. Rahman, L. C. L. Hollenberg, G. Klimeck, and M. Y. Simmons, Nat Nano **9**, 430 (2014).
[39] H. O. H. Churchill, F. Kuemmeth, J. W. Harlow, A. J. Bestwick, E. I. Rashba, K. Flensberg, C. H. Stwertka, T. Taychatanapat, S. K. Watson, and C. M. Marcus, Phys. Rev. Lett. **102**, 166802 (2009).
[40] H. O. H. Churchill, A. J. Bestwick, J. W. Harlow, F. Kuemmeth, D. Marcos, C. H. Stwertka, S. K. Watson, and C. M. Marcus, Nature Physics **5**, 321 (2009).
[41] G. A. Steele, G. Gotz, and L. P. Kouwenhoven, Nat Nano **4**, 363 (2009).
[42] T. S. Jespersen, K. Grove-Rasmussen, J. Paaske, K. Muraki, T. Fujisawa, J. Nygard, and K. Flensberg, Nat. Phys **7**, 348 (2011).

[43] J. Waissman, M. Honig, S. Pecker, A. Benyamini, A. Hamo, and S. Ilani, Nat Nano **8**, 569 (2013).
[44] A. Benyamini, A. Hamo, S. V. Kusminskiy, F. von Oppen, and S. Ilani, Nat Phys **10**, 151 (2014).
[45] R. A. Lai, H. O. H. Churchill, and C. M. Marcus, Phys. Rev. B **89**, 121303 (2014).
[46] M. C. Hels, B. Braunecker, K. Grove-Rasmussen, and J. Nygard, ArXiv:1606.01065 (unpublished).
[47] M. J. Yoo, T. A. Fulton, H. F. Hess, R. L. Willett, L. N. Dunkleberger, R. J. Chichester, L. N. Pfeiffer, and K. W. West, **276**, 579 (1997).
[48] M. Honig, J. A. Sulpizio, J. Drori, A. Joshua, E. Zeldov, and S. Ilani, Nat Mater **12**, 1112 (2013).
[49] G. Széchenyi and A. Pályi, Phys. Rev. B **88**, 235414 (2013).
[50] J. Danon, X. Wang, and A. Manchon, Phys. Rev. Lett. **111**, 066802 (2013).